

1

Introduction

Dispersed organic systems are ubiquitous in nature. Wood consisting of lignin and cellulose is a well-known example. A natural dispersion is blood that consists of plasma and dispersed organic cells. The main ingredient of the plasma is water and, therefore, its flow behavior is Newtonian. The organic cells of various shapes and compositions are distributed in the plasma and significantly influence the flow properties of blood.

Many of our food products consist of different ingredients not miscible with each other. Their flow properties play an important role either during processing or consumption. An example is dough whose main ingredients are a liquid like water or milk and dispersed flour particles. Dough is an extremely complicated material regarding its flow properties. Another example is chocolate, for which the flow behavior of a dispersed system plays a certain role for its production and for generating special tastes when eaten.

From daily life one knows toothpaste as a dispersed material that flows differently according to the forces applied: It is capable of being easily pressed out of a tube, but nearly rigid on the brush. Common particle-filled materials are paints and lacquers, printing inks, and cosmetic articles, for example. A special feature of these flowable systems is a low viscosity under load and a high one at rest. A dispersed material used in huge amounts worldwide is concrete, whose flow properties can become important when transported by pumping.

It should be mentioned that the dispersed component of a system can also be a gas or another liquid. The first composition is typical of foams, for the second, oily ingredients in water; milk, soaps, and creams are good examples.

All these materials are dispersions generally defined as mixtures of various ingredients that are not soluble with each other. Solid particles dispersed in a fluidic medium are called *suspensions*, immiscible liquids form an *emulsion*, and a system of liquid or solid particles in a gaseous medium is designated as an *aerosol*.

The matrices of most of these materials that form the base component of a dispersion have a low Newtonian viscosity, particularly in the case of water, which is often used as dispersing medium. A lot of investigations have already been performed on

dispersions based on water. Much less is known, however, on the flow properties of filled systems with matrices of higher viscosities than water or even of a non-Newtonian behavior. Such systems play an important role in the case of polymers that have found wide applications as engineering materials over the last decades. The products available on the market are numerous today. A great variety of organic and inorganic fillers mixed into various types of polymeric materials are in use. The fillers serve to improve properties of the matrices or to generate features the basic materials do not possess.

Another way of modifying existing products is blending them together to get new characteristics superior to those found for the components. Because only very few polymers are miscible with each other, most of the blends show a heterogeneous structure and can be considered as a dispersion in which both matrix and heterogeneous phase are of a polymeric nature. Such blends currently represent a big market in the field of engineering polymers.

Inherent to dispersed polymeric materials is the fact that optimizing one property by changing the composition alters other properties. This interplay has widely been investigated with respect to characteristics of the solid state, because they are interesting for applications. However, much less can be found in the literature on rheological properties, however, that may significantly be influenced by a component added to a matrix. Because the rheological behavior is a key factor for processing, it has to be balanced with respect to other material features required.

Nevertheless, the number of rheological textbooks in the field of dispersed polymeric materials is rather small. In one book, discussions on the rheology of polymer blends [1.1] are found, others are concerned with the rheology of filled polymers [1.2], [1.3]. Common books on rheology either do not deal with dispersed polymeric materials at all or only cover limited aspects, for example, [1.4], [1.5], [1.6].

The economic importance of filled polymeric materials and polymer blends and the very significant role that rheological properties play in their processing led to the conception of this book. Its main topics are related to polymers as the matrix that exhibit distinctly higher viscosities than water and are non-Newtonian in many cases. The discussion of particle-filled materials and polymer blends together in one volume offers the challenging chance to point out the similarities and differences of these two systems.

Besides rheological characterizations with respect to the different deformations and stresses occurring during processing, the other aspects dealt with are how rheological investigations can be used to get insight into interactions between structural heterogeneities themselves or interactions with matrix molecules. Another interesting field discussed in this book is the use of rheological measurements to follow up on morphological changes. Furthermore, the role of special flow fields in the molten state is elucidated for the generation of droplet distributions in polymer blends.

□ 1.1 References

- [1.1] Utracki L. A., *Polymer Alloys and Blends*, Hanser Verlag, Munich, Germany (1989)
- [1.2] Shenoy A. V., *Rheology of Filled Polymer Systems*, Kluwer Academic Publishers, Berlin, Germany (1999)
- [1.3] Leblanc H., *Filled polymers: science and industrial applications*, CRC Press, Boca Raton, Florida (2010)
- [1.4] Vinogradov G. V., Malkin A. Ya., *Rheology of Polymers*, Springer Verlag, Berlin, Germany (1980)
- [1.5] Macosko C. W., *Rheology: Principles, Measurements, and Applications*, Wiley-VCH, Weinheim, Germany (1994)
- [1.6] Münstedt H., Schwarzl F. R., *Deformation and Flow of Polymeric Materials*, Springer, Berlin, Germany (2014)

From the measured rotational velocity Ω and torque M of a cone-and-plate geometry with the cone angle β and the plate radius R , the shear viscosity can be determined. The cone-and-plate rheometer is a very versatile instrument insofar as it allows one to perform the experimental modes discussed before. For stressing experiments, the angular velocity is controlled, for creep experiments it is the torque. Dynamic-mechanical experiments can be carried out by applying either an oscillating torque or an angular displacement on the sample.

Despite all these advantages, cone-and-plate geometries have to be used with great care in the case of dispersed polymeric materials. Because the gap width decreases as the center of the cone-and-plate array is approached, particles may partially block the rotation and lead to wrong readings. Enlarging the gap width by increasing the cone angle and the truncation of the cone tip deteriorates the uniformity of the shear rate, which is just the advantage of the cone-and-plate geometry.

For completeness it may be mentioned that the first normal stress difference can be directly determined from the normal force (see [2.9]).

2.2.1.2 Plate-Plate Rheometer

The geometrical restriction of the gap width is less pronounced for the plate-plate assembly that is schematically presented in Fig. 2.5. Between the two parallel plates with radius R , the sample of the height H is placed. The distance of the plates H can be chosen in such a way that a hindrance of the rotation by particles can be avoided. The upper plate at $z = H$ may be driven with an angular velocity Ω and the resulting torque M measured at the lower plate.

Under the assumption of adhesion of the melt to the plates, the angular velocity ω in dependence on the distance z from the fixed plate follows as

$$\omega = \frac{\Omega}{H} z \quad (2.55)$$

and the shear rate at the position r becomes

$$\dot{\gamma} = \frac{dv_{\phi}}{dz} = \frac{d(r\omega)}{dz} = r \frac{d(\Omega z / H)}{dz} = r \frac{\Omega}{H} \quad (2.56)$$

Compared with the cone-and-plate device, the shear rate is not constant within the gap. It is zero at the rotation axis and reaches the maximum of

$$\dot{\gamma}_R = \frac{R\Omega}{H} \quad (2.57)$$

at the rim of the plate with radius R .

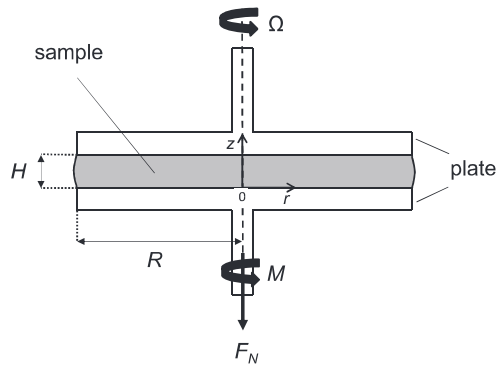


Figure 2.5 Plate-plate assembly: H : sample height, R : sample radius, Ω : angular velocity, M : torque, F_N : normal force. The cylindrical coordinate system is designated with z , r , and the azimuth angle Φ , which is not shown

According to Eq. 2.56, the shear rate for a fixed geometry of the plate-plate array is a linear function of r , and the stress distribution $\sigma(r)$ follows according to the rheological law. The integral moment M acting on the plate is given by

$$M = \int_0^R r dF = 2\pi \int_0^R r^2 \sigma(r) dr \quad (2.58)$$

considering that the force on a circular segment $2\pi r dr$ is $dF = 2\pi dr \sigma(r)$.

Introducing the new integration variable $\dot{\gamma} = \Omega r/H$, Eq. 2.58 becomes

$$M = 2\pi (H/\Omega)^3 \int_0^{\dot{\gamma}_R} \dot{\gamma}^2 \sigma(\dot{\gamma}) d\dot{\gamma} \quad (2.59)$$

For a further evaluation one needs the rheological law, that is, a relation between σ and $\dot{\gamma}$. In the simple case of a Newtonian liquid, $\sigma = \eta_0 \dot{\gamma}$ is valid and the torque follows as

$$M = \frac{\pi R^4}{2 H} \eta_0 \Omega = \frac{\pi R^3}{2} \eta_0 \dot{\gamma}_R = \frac{\pi R^3}{2} \sigma_R \quad (2.60)$$

with σ_R being the shear stress at the rim. From Eqs. 2.57 and 2.60, it is obvious that the radius of a sample has to be determined very carefully to get reliable values for the viscosity because inaccuracies propagate with the fourth power of R .

For a non-Newtonian fluid of an unknown rheological law the exact stresses can be determined experimentally, too, by a procedure similar to that applied in the case of shear rates for the capillary rheometer (see Section 2.2.2). The viscosity as a

function of shear rate can then be determined. For this purpose, an apparent shear stress σ_a at the rim is defined according to Eq. 2.60 by

$$\sigma_a = \frac{2M}{\pi R^3} \quad (2.61)$$

assuming a Newtonian viscosity. With M from Eq. 2.59 and $\dot{\gamma}_R$ from Eq. 2.57, the following relationship between the apparent shear stress σ_a and the true shear stress σ is obtained

$$\sigma_a = \frac{4}{\dot{\gamma}_R^3} \int_0^{\dot{\gamma}_R} \dot{\gamma}^2 \sigma(\dot{\gamma}) d\dot{\gamma} \quad (2.62)$$

Differentiation of the product $\sigma_a \dot{\gamma}_R^3$ with respect to $\dot{\gamma}_R$ leads to the equation that relates the true stress at the rim $\sigma(\dot{\gamma}_R)$ to the apparent stress σ_a

$$\sigma(\dot{\gamma}_R) = \sigma_a \left[\frac{3}{4} + \frac{1}{4} \frac{d \log \sigma_a}{d \log \dot{\gamma}_R} \right] \quad (2.63)$$

This equation has a structure similar to that of *Weissenberg and Rabinowitsch* (see Eq. 2.85). As the differential quotient in Eq. 2.63 comes to lie between 0 and 1 for polymer melts, it follows that

$$\frac{3}{4} \sigma_a < \sigma \leq \sigma_a \quad (2.64)$$

For Newtonian liquids the true stress is equal to the apparent stress, but it becomes smaller in the non-Newtonian region. With plate-plate devices, all modes described in Section 2.1 can be performed.

From the normal force exerted on the plates only the sum of the first and second normal stress coefficient can be directly determined [2.4]. Their separation requires measurements with different geometries that take a lot of effort and do not provide very accurate data.

2.2.1.2.1 Determination of Slip

The preceding formulas were derived under the assumption of adhesion of the melt to the plates. For highly filled suspensions, slip may occur, which leads to wrong rheological data if not taken into account. In the following it is shown that the slip velocity in a plate-plate geometry can quantitatively be determined by measurements at two different gap heights keeping the stress, that is the torque, constant (see [2.10]).

The occurrence of slip has the consequence that a finite slip velocity v_s at the two plates has to be taken into account, which may depend on the stress. At the rim an apparent shear rate $\dot{\gamma}_{aR1}$ can then be defined as

$$\dot{\gamma}_{aR1} = \dot{\gamma}_R + \frac{2v_s}{H_1} \quad (2.65)$$

with $\dot{\gamma}_R$ being the shear rate of the sheared material at the rim and H_1 the gap width. For an experiment with another gap width H_2 but at a constant shear stress, one gets

$$\dot{\gamma}_{aR2} = \dot{\gamma}_R + \frac{2v_s}{H_2} \quad (2.66)$$

because the viscosity and the slip velocity can be assumed to be a function of only the shear stress. Subtracting Eq. 2.66 from Eq. 2.65 results in the relation

$$v_s = \frac{\dot{\gamma}_{aR1} - \dot{\gamma}_{aR2}}{2(1/H_1 - 1/H_2)} \quad (2.67)$$

for the slip velocity v_s at a constant stress σ_R at the rim, that is, the torque has to be kept constant according to Eq. 2.61 when the gap width is changed. The apparent shear rates at the rim are obtained according to Eqs. 2.65 and 2.66.

By inserting v_s into Eq. 2.65 or 2.66, $\dot{\gamma}_R$ can be calculated and the viscosity follows

$$\eta = \frac{\sigma_R (H_1 - H_2)}{H_1 \dot{\gamma}_{aR1} - H_2 \dot{\gamma}_{aR2}} \quad (2.68)$$

2.2.1.2.2 Comparison of Plate-Plate (PP) and Cone-and-Plate (CP) Devices

1. The *sample preparation* for PP is easier than for CP devices. This feature may be of particular advantage in the case of filled polymeric materials.
2. The *shear rate* is approximately constant within the gap of CP, but is dependent on the position between the parallel plates of PP.
3. The *shear rate range* of PP is more variable than that of CP due to possible changes of plate diameter and gap width.
4. The *viscosity function* follows directly from the readings of CP, for PP a correction procedure has to be applied. This is not a problem, however, due to data processing.
5. CP has limitations in case of *particle-filled systems* due to acute-angled gap geometries.

□ 3.3 Interparticle Distances

An assessment of the interparticle distance IPD can be easily obtained in the simple case of systems filled with monodisperse spheres of the diameter d , which are uniformly distributed. The maximal packing density is designated as Φ_{\max} , whose value depends on the assumed packing geometry, of course. The particle concentration Φ is defined as

$$\Phi = \frac{V_p}{V_0} = N \frac{4\pi}{3} \left(\frac{d}{2}\right)^3 \frac{1}{V_0} \quad (3.6)$$

with V_p being the volume of the N particles in the total volume V_0 . The total volume can be imagined as the package of the N particles with the diameter d surrounded by a layer whose thickness is half of the interparticle distance IPD. The total volume of such particles with the diameter $d + \text{IPD}$ then follows as

$$V_0 = N \frac{4\pi}{3} \left(\frac{d + \text{IPD}}{2}\right)^3 \frac{1}{\Phi_{\max}} \quad (3.7)$$

and by introducing the particle concentration from Eq. 3.6 one gets

$$\Phi = \Phi_{\max} \left(\frac{d}{d + \text{IPD}}\right)^3 \quad (3.8)$$

or

$$\text{IPD} = d \left[\left(\frac{\Phi_{\max}}{\Phi}\right)^{1/3} - 1 \right] \quad (3.9)$$

In Fig. 3.4 the interparticle distances are presented for various particle sizes and maximum packing densities of $\Phi_{\max} = 0.524$ for a simple cubic, $\Phi_{\max} = 0.680$ for a face-centered cubic, and $\Phi_{\max} = 0.740$ for a hexagonal lattice. With increasing Φ , the interparticle distance becomes smaller and approaches zero for Φ approaching Φ_{\max} . Obviously, for very small concentrations the IPD formally grows asymptotically and loses any physical meaning with respect to particle interactions. For the chosen particle diameter $d = 1.2 \mu\text{m}$, interaction forces that may be assumed to act up to around 10 nm do not come into play at realistic volume concentrations up to 0.4 and the probability of entanglements between layered molecules of different particles is low even at coil diameters of 20 nm, which may be found in the case of polymers with high molar masses.

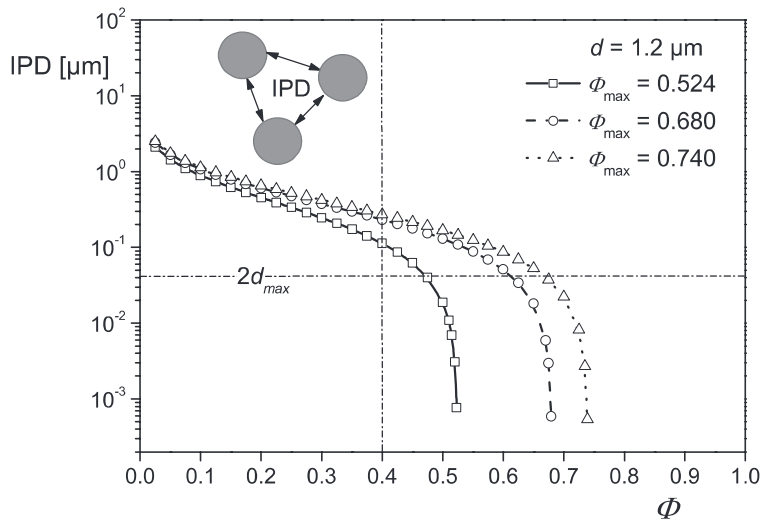


Figure 3.4 Interparticle distances IPD as a function of the volume concentration Φ for monodisperse spheres of a diameter $d = 1.2 \mu\text{m}$ and various maximum packing densities Φ_{max} according to Eq. 3.9 [3.3]. The d_{max} designates the maximum coil diameter assumed for polymer layers of high molar mass

It can be easily seen, however, from Eq. 3.9 that the IPD is proportional to the particle diameter and, therefore, interparticle interactions may play a dominant role for nanoparticles. For the case of a simple cubic packing of monodisperse spherical particles, that is, $\Phi_{\text{max}} = 0.524$, the IPD as a function of the particle diameter d is presented in Fig. 3.5 for various filler concentrations. For monodisperse particles with a diameter of 20 nm, for example, the IPD reaches the critical distance assumed to be around 10 nm for an efficiency of interparticle forces at concentrations around $\Phi = 0.1$. Entanglements between layered molecules that start to develop at IPD smaller than 40 nm may occur at about $\Phi = 0.01$, already, for particles of 20 nm diameter.

Regarding the effect of particle polydispersity on the IPD, a tendency can be deduced from Eq. 3.9. Because the maximum packing density becomes higher with increasing polydispersity [3.11], larger interparticle distances at a given concentration are to be expected.

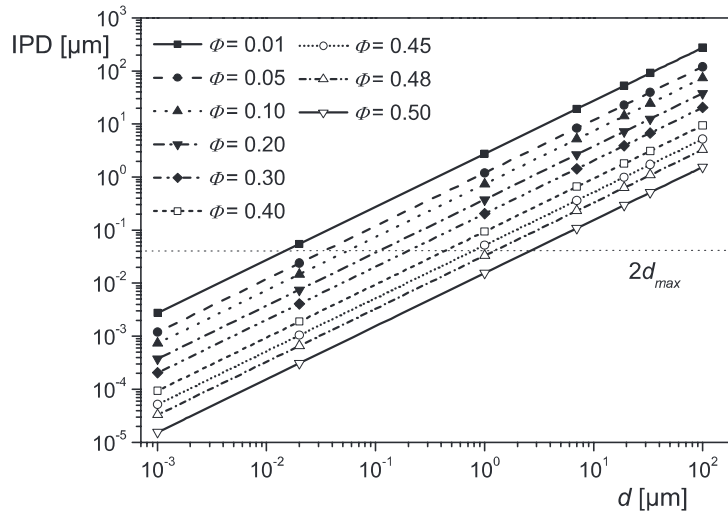


Figure 3.5 Interparticle distance IPD as a function of the particle diameter d at different filler concentrations for monodisperse spherical particles of a simple cubic packing ($\Phi_{\max} = 0.524$) [3.3]. The d_{\max} designates the maximum coil diameter assumed for polymer layers of high molar mass

□ 3.4 Sedimentation

Particles settle under gravity and, therefore, it is important for reliable rheological experiments on dispersed systems to be able to assess the sedimentation rate and to be aware of it when setting the measuring parameters. In the following a short discussion of the fundamentals of sedimentation and some results on various filled materials are given.

Stoke's law relates the velocity v of a sphere with the diameter d to the force F pulling it through a medium of the viscosity η under the conditions of laminar flow and negligible interactions with walls or other particles by

$$v = \frac{F}{3\pi d\eta} \quad (3.10)$$

Under gravity it follows

$$v = \frac{1}{18} \frac{\rho_s - \rho_M}{\eta} g d^2 \quad (3.11)$$

with ρ_S and ρ_M being the density of the sphere and the dispersing matrix fluid, respectively, and g the acceleration of gravity. In concentrated suspensions the settling of a particle is hindered by others resulting in smaller sinking velocities. Moreover, the sedimentation kinematics is affected by the shape of the particles and their distribution. Therefore, a direct measurement of the sinking velocities is necessary for a reliable assessment of the maximum experimental time to be applied. Because sedimentation of particles in a liquid cannot be practically avoided, conditions for acceptable measurements have to be set. For example, in the literature it is required that during an experiment a particle should not travel more than one tenth of the gap of the device used (see [3.14]).

Examples for sedimentation measurements on combinations of matrix and filler presented later are given in the following. The equipment used is rather simple. The suspension was filled into a cylindrical glass vessel whose diameter was around the factor 1000 larger than the average particle diameters in order to avoid an influence of the walls on the sedimentation process. The height of the column of the dispersed particles was measured then as a function of time.

As the matrix, a polyisobutylene with the zero-shear viscosity $\eta_0 = 10.4$ Pas at 31 °C was chosen. This viscosity is higher by about the factor 10^4 than that of water, for example, and according to Eq. 3.11, small sinking velocities compared to water should be expected.

The sedimentation experiments were carried out on suspensions with the particles listed in Table 3.1. C2, C3, and C5 are polydisperse silicate glass beads of different diameters, M 527 designates polymethylmethacrylate (PMMA) spheres with a diameter similar to that of C2, but a smaller dispersity index PDI.

Table 3.1 Specific Data of Particles of the Sedimentation Measurements; d_{50} is the average diameter of particle distributions, and PDI designates the polydispersity index [3.3]

Material	Name	r [g/cm ³]	d_{50} [μm]	PDI
Glass	C2	2.45	34	1.1
Glass	C3	2.45	7	1.3
Glass	C5	2.45	7	1.1
PMMA	M 527	1.16	33	1.5

As an example, sedimentation measurements on suspensions with three concentrations of the smallest glass beads are shown in Fig. 3.6. The height h of the column of the dispersion related to the height h_0 at the beginning of the sedimentation experiment is plotted as a function of the sedimentation time t_{sed} that stretches up to nearly 100 days. The height of the dispersion column decreases rapidly at short times and reaches a constant value later. The shapes of the curves are distinctly dependent on the concentration. The higher the concentration, the slower is the decrease. This finding is in agreement with the assumption that the sedimentation

7.2.3.2 Numerical Description of Viscosity Functions of Filled Thermoplastics with a Yield Stress

In a polymer melt that exhibits yielding, the acting total stress σ can be assumed to be the sum of the constant yield stress σ_y and the changing stress σ_{fl} effecting the flow. The viscosity formally follows then as

$$\eta = (\sigma_y + \sigma_{fl}) / \dot{\gamma} \quad (7.6)$$

If no yield stress exists or if the external stress applied to the melt is much larger than the yield stress, that means, $\sigma_{fl} \gg \sigma_y$, the flow behavior corresponds to that of a conventional unfilled melt governed by the shear thinning properties of the particular polymeric material. It may be then formally described by the Eqs. 7.4 or 7.5.

For a dominating yield stress, that means $\sigma_{fl} \ll \sigma_y$, one gets

$$\eta \cong \sigma_y / \dot{\gamma} \text{ or } \log \eta \cong \log \sigma_y - \log \dot{\gamma} \quad (7.7)$$

This equation is equivalent to a straight line with the slope of -1 in a double-logarithmic plot of η as a function of $\dot{\gamma}$. From the intercept, the yield stress can be determined. Typical examples of filled thermoplastics with a pronounced yielding behavior are displayed in Figs. 7.4 and 7.5. It should be mentioned that the slope of -1 in the double-logarithmic plot of a viscosity function is equivalent to a constant stress at the various shear rates.

When the yield stress σ_y and the stress σ_{fl} effecting the flow of the filled matrix in the hydrodynamic state are of the same order, their influences overlap each other and formally the viscosity function can be presented, for example, by

$$\eta(\dot{\gamma}) = \frac{\sigma_y}{\dot{\gamma}} + f(\dot{\gamma}) \quad (7.8)$$

If for $f(\dot{\gamma})$, the Ostwald de Waele law in the notation of Eq. 7.3 divided by $\dot{\gamma}$ is introduced, one gets

$$\eta(\dot{\gamma}) = \frac{\sigma_y}{\dot{\gamma}} + C\dot{\gamma}^{n-1} \quad (7.9)$$

or

$$\eta(\sigma) = \left(\frac{C}{\sigma - \sigma_y} \right)^{1/n} \sigma \quad (7.10)$$

Discussing the shear stress as a function of the shear rate leads to

$$\sigma = \sigma_y + C\dot{\gamma}^n \quad (7.11)$$

The Eqs. 7.9 to 7.11 are different versions of the Herschel-Bulkley equations [7.6]. The three parameters C , σ_y , and n have to be adapted to the data measured.

If for $f(\dot{\gamma})$ the Carreau-Yasuda formula is used, one gets

$$\eta = \frac{\sigma_y}{\dot{\gamma}} + \frac{\eta_0}{\left(1 + (\lambda\dot{\gamma})^a\right)^{k/a}} \quad (7.12)$$

Equation 7.12 may present a more accurate description than Eq. 7.9 when the measured viscosity function versus the shear rate shows a distinct change of curvature. The five coefficients σ_y , η_0 , λ , a , and k may formally be determined by a least-squares adaptation of Eq. 7.12 to the experimental curve. The physical meaning of the parameters is met better the more completely the different flow regimes are covered by the measurements. A rather formal description of experimental data by Eq. 7.12 may lead to unreasonable physical quantities.

At first glance, the fact that the coefficients of the Carreau-Yasuda formula of the matrix of the filled material could be determined experimentally seems to be an advantage for the numerical description of a filled polymeric system. But there are no theories or even rules from which a change of the coefficients by adding particles can be predicted. The influence of particles on η_0 is given by Einstein's formula (see Eq. 4.1) only for suspensions with properties that are far away from those of polymer melts. For the other parameters of Eq. 7.12, no relations are known that describe their change by adding fillers, therefore, Eq. 7.12 has to be considered as a complicated and rather formalistic description of viscosity functions of filled polymer melts.

An equation of the type

$$\eta(\dot{\gamma}) = \frac{\sigma_y}{\dot{\gamma}} + \frac{A}{1 + B\dot{\gamma}^{1-n}} \quad (7.13)$$

is reported in the literature to be successfully applied to the numerical description of a carbon black-filled compound with a yield stress [7.7]. Here, A and B are coefficients to be adapted and n stands for the power-law index. Again this equation is of an empirical nature and the coefficients are determined by a numerical fit.

For viscosity functions that do not show an obvious yield stress but a distinct viscosity increase at small shear rates, a polynomial according to Eq. 7.5 may be a pragmatic and simple description of viscosity functions to be used in modeling processing features or in screw design.

However, in cases where the determination of yield stress is of interest, simple relations like the empirical Herschel-Bulkley formula (see Eq. 7.11) or the Casson formula

$$\sigma^{1/2} = k_0 + k_1 \dot{\gamma}^{1/2} \quad (7.14)$$

are commonly applied. The Casson formula is based on the energy dissipation that is due to disintegration and rotational motions of chain-like particle agglomerates in laminar shear flow of Newtonian media [7.8]. These assumptions of the Casson equation have to be taken into account when it is applied to a numerical description of experiments.

The Bulkley-Herschel equation (Eq. 7.11) and the Casson equation (Eq. 7.14) both deliver the yield stress σ_y when extrapolated to $\dot{\gamma} = 0$. From Eq. 7.11, σ_y can be directly determined, in the case of an evaluation according to Equation 7.14 it follows $\sigma_y = k_0^2$. Principal differences between the two equations exist, however, at higher shear rates. For a negligible yield stress, the Casson equation describes a stress that is proportional to the shear rate, which means a Newtonian liquid, while the Herschel-Bulkley formula postulates a power-law increase of the shear stress with shear rate above the yield stress.

In the classical suspension rheology, the concept of the maximum volume fraction Φ_m plays an important role as discussed in detail in Chapter 4. The relationships between viscosity and filler concentrations based on Φ_m , like the Krieger-Dougherty equation (Eq. 4.11), are derived, however, for Newtonian matrices and fillers of regular shapes like spheres, for example. Both conditions are not fulfilled for the filled thermoplastics discussed in this chapter. The thermoplastic matrices generally show a pronounced shear thinning, particularly, under conditions of processing, and the fillers used in practice have aspect ratios that are commonly larger than one. Exceptions are beads or hollow glass spheres [7.9]. A typical picture of hollow spheres is shown in Fig. 7.6 together with micrographs of talc, calcium carbonate, and glass fibers.

Hollow glass spheres have recently attracted some interest with respect to applications because they exhibit similar beneficial effects on mechanical properties as compact spheres, but they obviously possess distinctly lower densities. Rheological measurements on thermoplastics with hollow spheres are very scarce in the literature up to now, however.

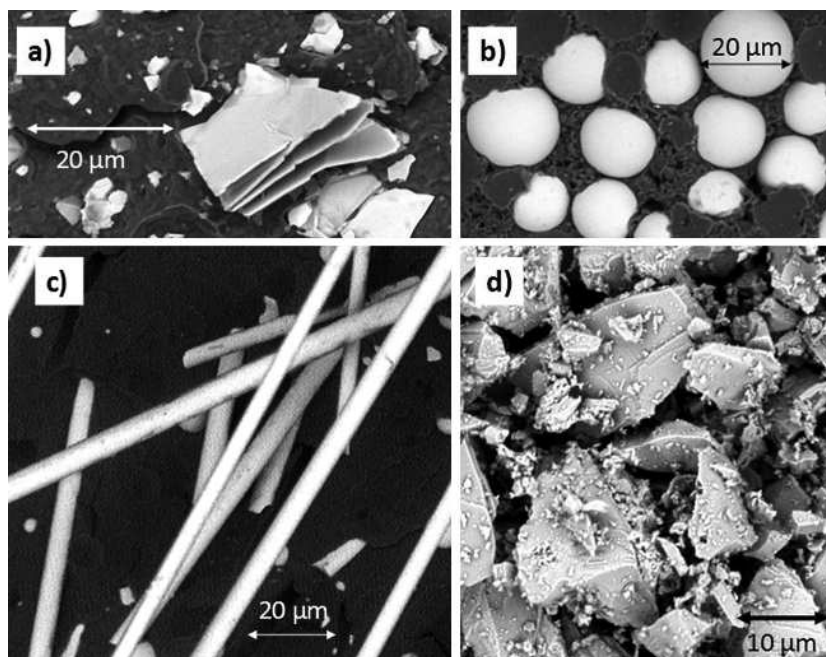


Figure 7.6 Micrographs of a) talc, b) hollow glass spheres, c) glass fibers, d) calcium carbonate [7.9]

□ 7.3 Entrance Pressure Losses

Besides viscosity functions, the entrance pressure losses of a polymer melt may be of interest in an assessment of pressure distributions within a tool, particularly if the length to radius ratio of ducts is small. An example is a pelletizing plate for which the entrance pressure loss may be significantly higher than the pressure loss in the holes of the plate caused by shear. Therefore, entrance pressure losses of filled thermoplastics are of interest if applications are concerned. In the literature, only a few reports are found because the accurate determination of entrance pressure losses using Bagley-plots requires a considerable experimental effort (see Section 2.2.2 and Fig. 2.10). The main reason for entrance pressure losses are pronounced elongation flows of polymer melts in narrowing ducts (see [7.10], for example). In Fig. 7.7 the entrance pressure losses p_e are plotted as a function of the wall shear stress σ for an unfilled PA 6 and a PA 6 filled with 30 wt.% glass beads or glass fibers with two different aspect ratios [7.1]. They were determined using a capillary rheometer with capillaries of radii 0.6 and 1.0 mm and L/R ratios between 1 and 50. The entrance pressure losses of the unfilled PA and the PA filled

with 30 wt.% glass beads are the same within the accuracy of the measurements, but the p_e of the fiber-filled samples are distinctly higher. Because the elongational deformation in the entrance region of a capillary covers a wide range of elongational rates changing locally and with time, relations between the elongational behavior of filled polymer melts discussed in detail in Chapter 8 and the entrance pressure losses are difficult to establish. It becomes obvious, however, that the entrance pressure losses of the fiber-filled polyamide samples in Fig. 7.7 are distinctly higher than those of the sample filled with the same content of glass beads.

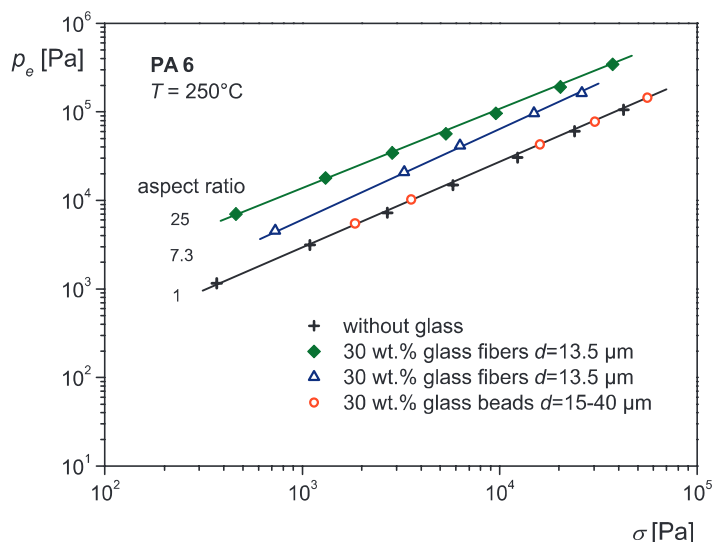


Figure 7.7 Entrance pressure loss p_e as a function of the shear stress σ at the wall of a capillary for the PA 6 matrix and PA 6 filled with 30 wt.% glass beads with diameters between 15 and 40 μm or glass fibers with mean values of 13.5 μm for the diameter and 25 or 7.3 for the aspect ratios, respectively. The temperature was 250 $^\circ\text{C}$ [7.1]

This finding can be explained by the assumption that the alignment of the glass fibers, which are randomly distributed in the barrel of the rheometer, by the extensional flow imposed on the melt in the entrance region of the capillary needs some energy that enhances the pressure loss. Taking this mechanism into account it seems to be reasonable that p_e becomes higher with a larger aspect ratio as it is obvious that a longer fiber exhibits a higher resistance against alignment in a viscous medium than does a shorter one.

In Fig. 7.8 the entrance pressure losses p_e , as functions of the shear stress σ at the wall of the capillary, are presented for an HDPE matrix and a compound filled with 30 wt.% of glass fibers. As for the samples in Fig. 7.7, which are based on PA 6, p_e of the fiber-filled HDPE is significantly higher than that of the matrix. Within the applied temperature range between 150 and 230 $^\circ\text{C}$, the pressure loss is the same

for the filled sample. A very similar behavior is reported for unfilled polymer melts that leads to the conclusion that the entrance pressure loss is mainly due to elastic effects being temperature independent in good approximation (see [7.10], for example). For dominating viscous processes, a distinct temperature dependence should be expected.

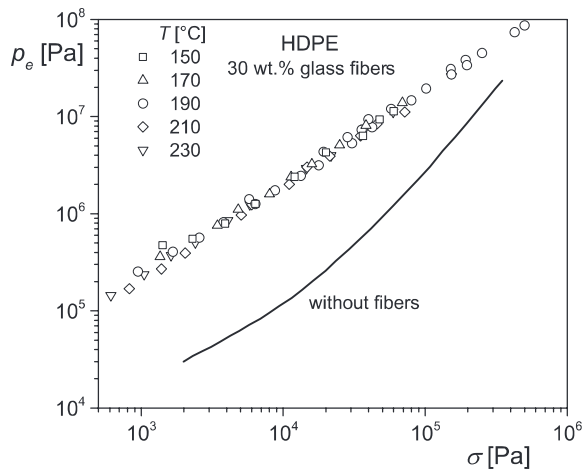


Figure 7.8 Entrance pressure loss p_e as a function of the shear stress σ at the wall of a capillary for a HDPE matrix and its compound with 30 wt.% glass fibers at different temperatures [7.1]

□ 7.4 Elastic Effects

Elasticity is an essential rheological property of polymer melts. Some fundamentals regarding the definition and determination of elastic quantities and their relations with the molecular structure of neat thermoplastic polymers are given, for example, in [7.10]. Much less is known about the elastic effects of filled thermoplastics. Whereas elastic properties in the linear range of deformation were used in previous sections of this book to get an insight into the structure buildup (see Sections 4.2.3, 5.3.2 and 5.3.4), for the processing of filled thermoplastics, the nonlinear range is of special interest.

7.4.1 Extrudate Swell

An obvious nonlinear elastic effect is the extrudate swell, which may be determined according to

8

Elongational Properties of Filled Thermoplastics

As shown in the previous chapters, the rheological properties of filled polymeric materials in shear can markedly differ from those of their matrices. These results provoke the question in what way the elongational behavior of thermoplastics is affected by various fillers.

□ 8.1 Elongational Viscosity of Unfilled Polymers

Elongational properties of unfilled polymer melts have received a lot of attention during the last 40 years because their behavior can be totally different from that in shear, as demonstrated by Fig. 8.1 for a low-density polyethylene. The shear viscosity increases with time and approaches a plateau that depends on the shear rate.

In the nonlinear range the steady-state viscosity becomes higher with decreasing shear rate. The linear range is characterized by the time-dependent viscosity $\eta^0(t)$ being independent of shear rate. At low elongational rates or short experimental times, the time-dependent elongational viscosity $\eta_E(t) = \sigma(t)/\dot{\epsilon}$ defined by Eq. 2.7 runs parallel to the time-dependent linear shear viscosity. The viscosity $\eta_E^0(t)$ is three times higher than $\eta^0(t)$. This relation is known as the Trouton ratio. At larger elongational rates, the elongational viscosity of the LDPE in Fig. 8.1 shows a sharp upswing that occurs at shorter times the higher the rate. This viscosity increase is commonly called *strain hardening*. At longer times or higher strains, the elongational viscosity seems to approach a plateau. Detailed information on elongational properties of unfilled polymer melts can be found in [8.3], for example.

Strain hardening is not a general feature of all polymer melts, as the measurements in Fig. 8.2 on a standard polypropylene designated as PP-0 demonstrate.

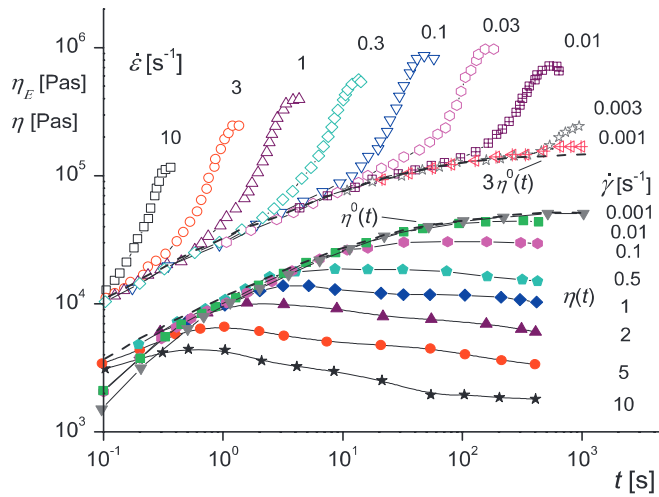


Figure 8.1 Elongational viscosity η_E and shear viscosity η as functions of time t for a low-density polyethylene at different elongational rates $\dot{\epsilon}$ and shear rates $\dot{\gamma}$ (reprinted from [8.1] with permission from Wiley and Sons and from [8.2] with permission from Springer Science+Business Media)

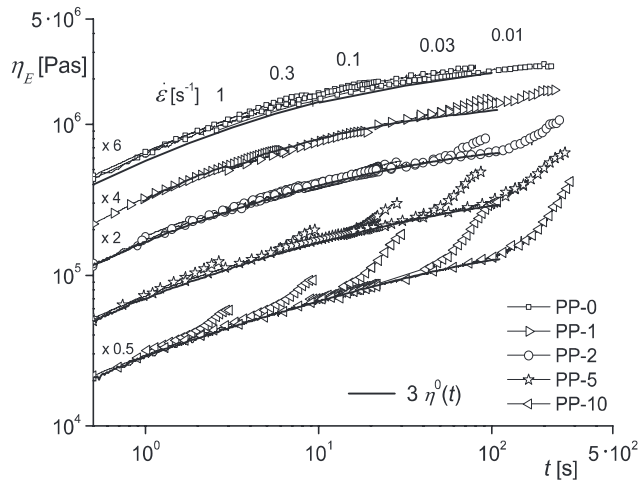


Figure 8.2 Elongational viscosity η_E as a function of time t at various elongational rates $\dot{\epsilon}$ for a standard polypropylene and various long-chain branched polypropylenes obtained by electron beam irradiation. The numbers of the sample designations indicate the different irradiation doses in kGy. The digits on the curves are the factors by which the curves were shifted with respect to PP 5 for a better visualization (reprinted with permission from [8.4], copyright 2008 American Chemical Society)

At all of the elongational rates applied, the viscosities come to lie on one curve, and an indication of strain hardening is not seen up to the measured total Hencky strains of about $\varepsilon = 4$, which corresponds to a stretching ratio of around $\lambda = 50$ (see Eq. 2.5). However, the other samples in Fig. 8.2 do exhibit strain hardening. They were obtained by electron-beam irradiation, which generates long-chain branches as described in [8.4]. The strain-hardening effect becomes more pronounced the higher the irradiation dose, which is indicated in kilograys (kGy) by the digit of the sample designation. Using size exclusion chromatography (SEC) coupled with multi-angle laser light scattering (MALLS), it could be shown that the degree of long-chain branches increases with the irradiation dose [8.4]. Taking these results and those on various polyethylenes into account (see Fig. 8.1 and [8.3], for example), long-chain branching could be assumed as the source of strain hardening.

This conclusion is too simple, however, as the results of Fig. 8.3 on various linear polystyrenes show, whose molar mass distributions are presented in the inset [8.5]. For the very narrowly distributed anionic polystyrene PS III, strain hardening could not be detected. However, the anionic polystyrene PS II exhibits a distinct strain hardening. The molar mass distribution of PS II is distinguished from that of PS III by a small high molar mass component that is clearly separated from the main peak. The results from [8.6] on long-chain branched polystyrenes and on blends of various linear PS, which exhibit strain hardening, demonstrate that even for one material, the feature of strain hardening can have its origin in different molecular structures.

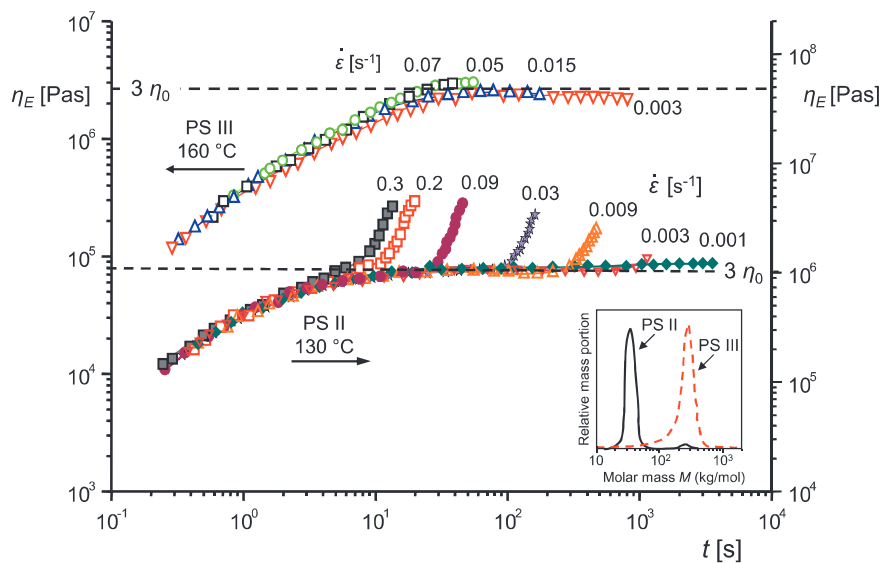


Figure 8.3 Elongational viscosity η_E as a function of time t for polystyrenes with various molar mass distributions (reprinted with permission from [8.5]; copyright 1980, The Society of Rheology)

Rheological properties are markedly affected by molecular motions, which are reflected by the retardation or relaxation time spectrum. The introduction of long-chain branches or the addition of molecules of a distinct high molar mass lead to long relaxation times, which can be assumed to be the reason for the increase of the elongational viscosity as a function of time. These results find their equivalence in the enhancement of elastic quantities, when distinctly higher molar mass components are added to a matrix or long-chain branches are introduced (see [8.7], for example).

□ 8.2 Elongational Viscosity of Filled Polymers

An interesting question is how elongational properties of filled polymeric materials might be derived from those of their matrices. The finding that fillers may be the origin of long retardation times affecting the linear behavior as shown in Section 5.3.5, makes it worthwhile to discuss whether they initiate strain hardening, in analogy to the postulated effect of long relaxation times of unfilled strain-hardening polymer melts.

Besides addressing this more fundamental question, elongational measurements have a very practical rheological aspect. They are mostly performed on free-standing samples and, therefore, slip on the wall of a rheometer, possible in shear, is not an issue. Because filled polymer melts are prone to slippage, experimental artifacts due to slip may be avoided by characterizing melts in extension. Last but not least, elongational experiments may help to understand certain aspects of the processing of filled thermoplastic materials that include extensional components. An example is the extrudate swell.

Elongational measurements on filled thermoplastic materials are rather scarce in the literature. For example, in [8.8] it is reported that for a polystyrene filled with 30 vol.% calcium carbonate, the time-dependent elongational viscosity is distinctly higher than that of the matrix. This effect is not unexpected at all, because from shear experiments, the effect of fillers enhancing the viscosity of a matrix is well-known. In addition, the general feature of the viscosity curves changes. Whereas for the unfilled polystyrene, a weak strain hardening is reported, the time-dependent elongational viscosity of the filled sample is found to lie below the curve in the linear regime. In analogy to the decrease of the shear viscosity with shear rate, which is commonly called *shear thinning*, such a behavior is designated "*strain thinning*." This effect is more pronounced the larger the strain rate applied. A similar result was presented in [8.8] for polystyrene with titanium dioxide. However, the results are only of rather limited value because any information about the

□ 14.4 Models for Particle Interactions in Rubber-Filled Styrene-Acrylonitrile Copolymers

The morphologies of the ASA and the ABS with about 40 wt.% of rubber look totally different. From Fig. 14.10 one can imagine that the acrylic ester particles of the ASA form agglomerates, building up a cage-like structure with inclusions of the SAN matrix molecules. The morphology of the ABS (see Fig. 14.1) cannot be described by such a picture. Rather, structures can be worked out of rubber particles arranged like pearls on a string with small distances between them. Such structures are particularly obvious for the smaller particles. A model for the ASA is sketched in Fig. 14.15. The rubber particles with a diameter of about $0.3\ \mu\text{m}$ form the walls of the cells that surround the matrix molecules with a diameter of around 25 nm.

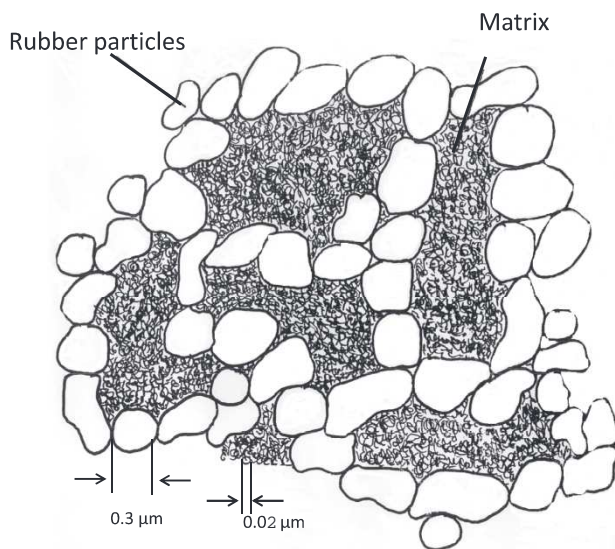


Figure 14.15 Model for the structure of the rubber particles in ASA

The attractive forces between the particles can be assumed to be of a polar nature. It is obvious from this model that the motions of the matrix molecules are hindered as long as the walls formed by the rubber particles are intact. This simple picture makes plausible the existence of a yield stress for ASA shown in Fig. 14.11. It is very easy to imagine that under certain stresses the walls formed by the particles can break down and the matrix molecules are able to flow freely. The structure breakdown of the rubber particles of the ASA with 40 wt.% acrylic ester is demon-

strated by the electron micrographs of Fig. 14.16. The left-hand electron micrograph shows the morphology of the ASA sample at rest. Cage structures are distinctly visible. The right-hand picture presents the morphology within a strand quenched after extrusion through the die of a capillary rheometer at an apparent shear rate of 100 s^{-1} . The walls no longer exist, but the particles are aligned in the direction of flow that is indicated by the arrow. It is obvious that the matrix molecules can move over long distances now, and this change in molecular mobility is reflected by a shape of the viscosity function at higher shear rates or shear stresses, respectively, that is typical of unfilled polymer melts (see Fig. 14.11).

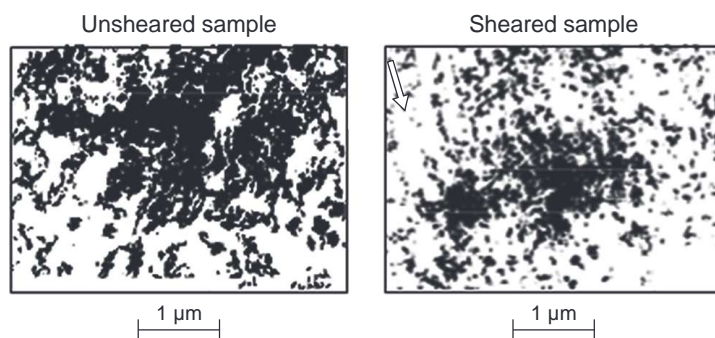


Figure 14.16 Electron micrographs of the unsheared ASA with 40 wt.% rubber (left) and the same material extruded through a capillary at an apparent shear rate of 100 s^{-1} (right). The arrow in the right-hand picture indicates the direction of flow (reprinted from [14.1] by permission from John Wiley and Sons)

The model proposed for the ASA is very similar to that discussed in Section 4.2.1 for PMMA beads of an average diameter of $30 \mu\text{m}$ and a volume concentration of 30% in the Newtonian polyisobutylene. For this suspension, it was demonstrated by in situ optical investigations during shear in a plate-plate geometry that a cell structure built up by the particles at rest can be destroyed, and an alignment of the beads occurs. The corresponding model is sketched in Fig. 4.3.

For the ABS with 43 wt.% rubber, the model of cells whose walls are formed by the rubber particles is not obvious from the structures shown in Fig. 14.1. Rather, it may be assumed that the particles are able to form a continuous network within the matrix if the interparticle distance (IPD) is smaller than twice the coil diameter of the SAN molecules grafted to the rubber surface and entanglements become possible (see Fig. 3.3).

The model corresponding to this assumption is sketched in Fig. 14.17. The sizes of 0.1 and $0.4 \mu\text{m}$ represent the small and large particles of the ABS investigated. The average diameter of the grafted SAN molecules of around 25 nm was assessed from the simple correlation existing between the molar mass of a molecule and its

dimension in theta solution (see for example [14.3]). In addition, use is made of the experimental finding that the geometry of a molecule in the molten and solid state can be considered to be the same as in theta solution.

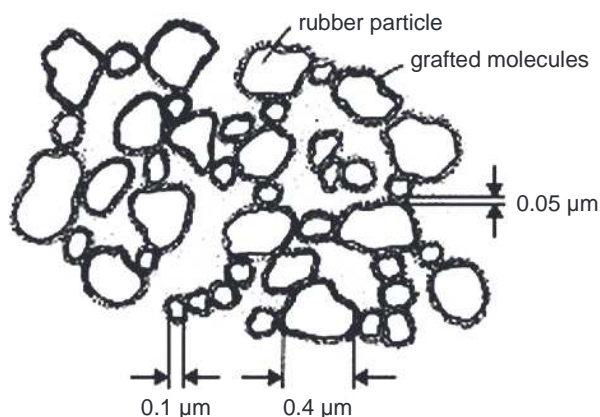


Figure 14.17 Simplified model of the structure of the ABS presented in Fig. 14.1. The grafted molecules are represented by a layer of $0.025\ \mu\text{m}$ surrounding the particles. The SAN matrix molecules are located within the loops of the network built up by the particles with grafted molecules

An assessment of the interparticle distances (IPD) follows from a simple geometrical consideration displayed in Section 3.3 and visualized by Fig. 3.5. The dependence of the interparticle distance on the particle diameter is presented there for different particle concentrations under the assumption of a simple cubic packing of the particles. As is seen from Fig. 3.5, an IPD of $50\ \text{nm}$ corresponding to the diameters of two grafted molecules may be reached at a volume ratio of $\Phi = 0.2$ for the particles $0.1\ \mu\text{m}$ in diameter and at $\Phi = 0.4$ for the particles with $0.4\ \mu\text{m}$. Around these concentrations, a distinct viscosity increase at small shear stresses, indicating a hindrance of the flow of matrix molecules, is found in Fig. 14.3. Although this assessment is somewhat simplified in the case of the real structure of the ABS, it nevertheless shows that a bridging of interparticle distances by the grafted molecules is not fictitious. Because the molar masses of the molecules are high enough to form entanglements, one can imagine that a network of particles interconnected by entangled grafted molecules exists throughout the sample that hinders the mobility of the molecules and gives rise to a yield stress. Molecular motion becomes possible again when the applied stress is high enough for disentanglements. Then the viscosity function becomes similar to that of the matrix, being somewhat higher only due to the hydrodynamic effect of the fillers.

From this model it is obvious that a yield stress does not exist at lower concentrations, where the distances between the particles become so large that they cannot be bridged by the grafted molecules anymore.

It should be pointed out that a yielding behavior can be found for monomeric fluids filled with inorganic particles, too. For these suspensions, the cell model sketched in Fig. 14.15 has to be considered because monomers or even oligomers are too small to be able to bridge the gaps between particles.

□ 14.5 References

- [14.1] Münstedt H., Rheology of rubber-modified polymer melts, *Polym. Eng. Sci.*, 21 (1981) 259–270
- [14.2] Bousmina M., Muller R., Rheology/morphology/flow condition relationships for polymethylmethacrylate/rubber blend, *Rheol. Acta*, 35 (1996) 369–381
- [14.3] Münstedt H., Schwarzl F.R., Deformation and Flow of Polymeric Materials, Springer, Heidelberg, Germany (2014)
- [14.4] Takahashi T., Wu W., Toda H., Takimoto J., Akatsuka T., Koyama K., Elongational viscosity of ABS polymer melts with soft or hard polybutadiene particles, *J. Non-Newtonian Fluid Mech.*, 68 (1997) 259–269
- [14.5] Meissner J., Development of a universal extensional rheometer for the uniaxial extension of polymer melts, *Trans. Soc. Rheol.*, 16 (1972) 405–420
- [14.6] Zosel A., Viskoelastisches Verhalten von ABS-Polymeren in der Schmelze, *Rheol. Acta*, 11 (1972) 229–237

Index

A

- acrylonitrile-butadiene-styrene copolymers (ABS) 305, 306
 - dynamic-mechanical experiments 316
 - electron micrographs 306
 - interparticle distance 306, 321
 - morphology 306
 - rheological properties 305
 - structure 306
 - viscosity functions 307
- acrylonitrile-styrene-acrylicester copolymers (ASA) 314
 - morphology 314
 - rheological properties 314
 - viscosity functions 315
- aerosol 1
- amorphous polymers 223
 - polycarbonate (PC) 223
 - polyvinylchloride (PVC) 223
- anisotropy of particle distributions
 - full width at half the maximum of the intensity peak (FWHM) 402
 - recovery experiment 402
 - relaxation experiment 401
 - X-ray diffraction 442
- Arrhenius equation 17
- Arrhenius plot 67
- atomic force microscopy (AFM)
 - micrographs 422
 - morphological investigations 445

B

- Bagley correction 30
- blend morphology
 - influence of sample preparation 430
- blends of high-temperature resistant polymers 274

- PEKEKK/PEI 276
- PEKEKK/PES 274, 276
- blends of LLDPE and PP 282

C

- capillary flow
 - fibril formation 366
 - Newtonian fluid 363
 - non-Newtonian fluid 363
- capillary number 264, 379, 386
 - in elongation 265
 - in shear 265
- carbon black 145, 146
 - morphology 147
 - properties 146
- carbon nanotubes 164
- carbon nanotubes in PMMA
 - electron micrographs 251
 - recoverable compliance 252
 - solution mixing 251
- carbon nanotubes in PP 252
 - creep compliance 254
 - preparation techniques 252
 - recoverable compliance 254
- Carreau-Yasuda formula 180
- Casson formula 184
- Casson-plot 196
- characterization of sample morphology 438
 - PS/LLDPE 438
 - SAN/PP 442
- coalescence 268, 389
- cocontinuous blends PS/LLDPE 344
 - elongational viscosity 346
 - extrudate swell 345
- coil radius 54
- Cole-Cole plot 283
 - temperature dependence and miscibility 283

- compatibilization 349
 - morphology development 413
 - particle size 420
 - physical compatibilization 350
 - reactive compatibilization 353
 - compatibilized blends
 - cryogenic smoothing 412, 440
 - compatibilized PS/LLDPE
 - elongational properties 351
 - rheological properties 349
 - compatibilized PS/PMMA
 - morphology development 407
 - particle size 409
 - compatibilized PS/PP
 - storage modulus 354
 - viscosity functions 355
 - compatibilizer 256
 - distribution on interface 412
 - particle size 415
 - complex viscosity
 - polystyrene blends 289
 - compliance 8
 - complex 14
 - creep 9
 - recoverable 8
 - steady-state recoverable 9
 - cooling time
 - influence on morphology 439
 - Cox-Merz rule 15, 152, 326
 - filled samples 100
 - creep and creep-recovery 246
 - linearity 247
 - stationarity 246
 - creep compliance 63
 - PMMA/carbon nanotubes 166
 - PMMA/graphite 161
 - PMMA/nanoclay 141
 - PMMA/nanosilica 106
 - creep experiments in elongation 335
 - creep recovery compliance 64
 - PMMA/nanosilica 106
 - critical capillary number 266
 - elongation 266
 - shear 266
 - crystallinity
 - PC 235
 - PVC 228
 - crystallization of PC
 - dependence on filler 238
 - dependence on processing 238
 - modulus increase with time 236
 - cumulative particle distribution
 - recovery experiment 399
 - relaxation experiment 397
- D**
- decay time of fibrils 394
 - determination of droplet distributions 433
 - determination of morphology
 - freezing of samples 439
 - differential scanning calorimetry (DSC)
 - heat flux of PC 235
 - heat flux of PVC 228, 234
 - melting enthalpy of different PC 239
 - dipole-dipole interaction 261
 - dispersed polymeric materials 2
 - dispersion 1
 - dispersion of nanosilica 116
 - droplet breakup 267
 - droplet deformation 264
 - critical capillary number 369
 - Grace curve 369
 - planar extension 369
 - shear 368
 - Taylor's experiments 368
 - dynamic-mechanical experiments 12
 - ABS with various rubber content 316
 - amplitude dependence 86
 - comparison PS and PVC 226
 - comparison with creep 106
 - extension of frequency range 113
 - frequency dependence 86
 - immiscible polymer blends 323
 - influence of nanosilica 103
 - loss modulus 86
 - storage modulus 86
 - styrene-acrylonitrile copolymer 316
 - dynamic-mechanical thermal analysis (DMTA)
 - PS/PPE blend 273
 - dynamic percolation 156
- E**
- Einstein equation 51, 183
 - elastic behavior 61
 - creep-recovery 62
 - electrical conductivity
 - amplitude dependence 156
 - carbon black 154
 - carbon black concentration 156
 - PMMA/graphite 161

- electron micrographs and X-ray patterns
 - uncompatibilized and compatibilized PS/LLDPE 414
 - electron microscopy
 - compatibilized blends 440
 - cryogenic fracture 438
 - uncompatibilized blends 438
 - elongational measurements
 - creep experiments 210
 - uniformity of deformation 210
 - elongational properties 203
 - compatibilized PS/LLDPE 351
 - filled thermoplastics 203
 - elongational viscosity
 - ABS 313
 - filled polymers 206
 - high molar mass component 295
 - influence of particle shape 208
 - long-chain branched polypropylene 204
 - low-density polyethylene 203
 - PMMA/nanoclay 209
 - PMMA/SAN 334
 - polypropylene blends 301
 - polystyrene 205
 - polystyrene blends 296
 - SAN/UHMW-PS 334
 - unfilled polymers 203
 - emulsion 1
 - energies of interaction 258
 - entanglements 43
 - enthalpy 256
 - entrance flow 364
 - entrance pressure loss 30
 - filled polymers 185
 - HDPE/glass fibers 187
 - PA/glass fibers 186
 - entropy 256, 257
 - extrudate swell 27, 64, 134, 187
 - ABS 310
 - comparison blend/filled polymer 332
 - HDPE/glass fibers 188
 - influence of nanofillers 101
 - PMMA/nanoclay 220
 - PP/glass fibers 188
 - PS/LLDPE 330
 - PVC and PS in comparison 231
 - SAN/PP 330
- F**
- fibril breakup 267
 - end pinching 268
 - necking 267
 - Rayleigh breakup 267
 - fibril decay 419
 - compatibilizer 416
 - fibrillar structure 387
 - fibrillation 387
 - filled polymers
 - elongational properties 203
 - general properties 173
 - Newtonian behavior 51
 - non-Newtonian behavior 55
 - recoverable elongation 217
 - Flory-Huggins parameters 259
 - flow curves
 - PVC and PS in comparison 231
 - flow profiles
 - PVC and PS 229
 - full width at half the maximum of the intensity peak (FWHM) 443
- G**
- Gibbs free energy of mixing 256, 258
 - glass beads 56
 - glass transition temperature of blends
 - Fox equation 273
 - linear mixing rule 273
 - Grace curve 266, 387
 - limitations for engineering polymers 370
 - grafted molecules 115
 - grafted silica particles
 - nuclear magnetic resonance (NMR) 114
 - graphene 163
 - graphite 159
- H**
- Hencky strain 7
 - Herschel-Bulkley equations 183
 - Herschel-Bulkley plot 197
 - high-impact polystyrenes 305
 - high-temperature resistant polymers
 - chemical structure 274
 - Hildebrand solution parameters 260
 - hydrodynamic forces 69
 - hydrogen bonding 261
- I**
- immiscible polymer blends
 - dynamic-mechanical experiments 323
 - logarithmic mixing rule 328

- morphology development 363
- rheological properties 323
- interaction energies 259
- interfacial tension 325
 - compatibilizer 415
 - methods for determination 436
- internal energy 256
- interparticle distance IPD 42–46, 113

K

- Krieger-Dougherty equation 53, 78, 79

L

- lattice approach (Flory, Huggins) 257
- LDPE/glass beads
 - elongational viscosity 216
 - shear viscosity 215
- linear elastic quantities 329
- linear polyethylenes
 - miscibility 297
 - zero-shear viscosity 297
- linear steady-state recoverable compliances
 - high molar mass component 293
 - mixing rule 290
 - polyisobutylene blends 293
 - polystyrene blends 293
- logarithmic mixing rule 287
 - polystyrenes 289
- logarithmic normal distribution function
 - SAN/PP 435
- loss modulus
 - influence of carbon black 151

M

- Marangoni stresses 411, 416
- master curves of ABS 309
- maximum packing densities 44, 79
 - influence of polydispersity 80
 - various methods for determination 79
- measurement of recoverable compliance 244
 - drift correction 245
 - recovery curves 244
- micrographs of various fillers 185
- miscibility 260, 261
 - electron microscopy 261
 - experimental methods 261
 - glass transition 261, 271
 - linear and long-chain branched polyethylenes 299
 - linear polyethylenes 297

- scattering methods 261
- thermorheological behavior 262
- thermorheological properties 278
- turbidity 261
- miscible blend
 - polystyrene/polyphenylene ether (PS/PPE) 271
- mixing behavior
 - PIB/PDMS 327
- mixing enthalpy 258
- mixing entropy 257
- mixing rule
 - complex viscosity 288
 - linear steady-state recoverable compliance 290
 - zero-shear viscosity 285, 286
- model for ABS 320
- model for ASA 319
- model for particle-filled polymers 113
 - coil diameter 113
 - detachment of molecules 134
 - thermal analysis 115
- model of strain-thinning 214
- modulus
 - complex 13
 - loss 13
 - plateau 14
 - storage 13
- morphological changes 2
- morphologies 165
 - carbon black 155
 - carbon nanotubes 165
 - graphite 159
 - PS/LDPE compared to PS/LLDPE 378
 - SAN/PP blends 331
- morphologies of elongated PA/SAN
 - influence of compatibilizer 423
- morphology development 392
 - circular die 363
 - compatibilized polymer blends 407
 - compatibilized PS/PMMA 409
 - conclusions from rheology 371
 - constant elongational rate 375
 - constant tensile stress 385
 - Hencky strain 377
 - immiscible blends 363
 - immiscible Newtonian liquids 367
 - indirect determination of parameters 370
 - planar extension 367
 - PMMA/PS 365
 - PS/LLDPE 376
 - recovery experiment 398

- relaxation and recovery 392
- relaxation and recovery of SAN/PP 400
- relaxation experiment 396
- role of elongational experiments 371
- simple shear 367
- single droplets 368
- morphology development in elongation
 - dependence on capillary number 382
 - dependence on composition 382
 - dependence on strain rate 381
 - dependence on temperature 380
 - SAN/PP 389
- morphology development under constant capillary number
 - PS/LLDPE 386
- morphology development under constant stress
 - SAN/PP 90/10 391
- morphology during relaxation
 - compatibilization 417
- morphology of ASA
 - influence of shear 320
- morphology of blends 263
- morphology of compatibilized blend
 - influence of shear rate 420
- morphology of compatibilized PA/SAN
 - influence of compatibilizer concentration 422
 - role of capillary number 425
- morphology of compatibilized PS/PMMA
 - influence of compatibilizer content 410
- morphology of PA/SAN
 - influence of compatibilizer on droplet geometry 424
- morphology of PS/LLDPE 340
 - influence of elongation 340
 - recovery after elongation 341
- morphology of PVC 227

N

- nanoclay
 - dispersion 138
 - exfoliation 138
- nanoclay in PMMA
 - exfoliation 248
 - melt mixing 248
 - recoverable compliance 249
 - storage modulus 250
- nanoparticles
 - effect on processing properties 99
 - effect on rheological properties 93
 - effect on viscosity functions 100
- nanosilica
 - dynamic-mechanical experiments 103

- polymethylmethacrylate 96
- polystyrene 94
- normal stress difference 64
 - filled polymers 189
 - first 11
 - polystyrene/calcium carbonate 189
 - second 11
- number-average particle distribution functions
 - effect of deformation modes 399
- numerical description of viscosity functions
 - filled thermoplastics 182

O

- Ostwald de Waele law 180

P

- packing densities 53, 79
- Palierne model 323
 - PA/SAN blend 325
 - PC/PS 325
 - PC/SAN 325
 - PS/SAN 325
- particle characterization
 - distribution density 434
 - logarithmic normal distribution function 434
 - number average 433
 - volume average 433
- particle distribution
 - cumulative 39
 - laboratory kneader 431
 - PS/LDPE 379
 - PS/LLDPE 379
 - SAN/PP 95/5 and 90/10 389
- particle-filled wax 192, 198
 - adhesion to wall 193
 - Casson formula 195
 - composition 193
 - Herschel-Bulkley formula 195
 - processing properties 200
 - structural features 199
 - viscosity functions 193, 194
 - yield stresses 198
- particle size average
 - number 40
 - volume 40
- PA/SAN blends
 - effect of compatibilizer on elongational viscosity 358
 - influence of compatibilizer on recoverable elongation 359

- Payne effect 136
 - PEKEKK/PEI blends
 - Fox equation 276
 - loss tangent 276
 - PEKEKK/PES blends
 - electron micrograph 277
 - heat flux 274
 - loss tangent 276
 - percolation curve
 - PMMA/carbon nanotubes 167
 - PP/carbon nanotubes 170
 - percolation threshold 154, 157
 - physical compatibilization
 - capillary number 419
 - plate-plate rheometer
 - electrical conductivity 24
 - polydispersity factor 41
 - polydispersity index 40
 - polyethylenes
 - miscibility 299
 - polyisobutylene blends
 - linear steady-state recoverable compliance 294
 - zero-shear viscosity 294
 - polyisobutylene (PIB) 56
 - polymer blends 2, 255
 - homologous components 285
 - linear and long-chain branched polypropylenes 300
 - miscible 256
 - nonmiscible 256
 - rubber-filled polymers 305
 - polymer droplet deformation
 - comparison with Taylor's theory 373
 - effect of viscosity ratios 374
 - uniaxial elongation 372
 - polymer melts with intrinsic structural heterogeneities 223
 - polymer solution 53
 - polymethylmethacrylate/polystyrene blend (PMMA/PS) 324
 - polynomial for viscosity functions 181
 - polypropylene blends
 - elongational viscosities 302
 - logarithmic mixing rule 301
 - strain hardening 302
 - viscosity functions 300
 - polystyrene 285
 - blends 285
 - calcium carbonate 174
 - glass beads 174
 - zero-shear viscosity 286
 - polystyrene blends
 - linear steady-state recoverable compliance 292
 - polyvinylchloride (PVC)
 - internal structures 224
 - rheological properties 224
 - power-law index 180
 - preparation of carbon nanotube composites
 - in situ polymerization 243
 - solution mixing 243
 - processing of ABS 308
 - processing of conducting thermoplastics 157
 - PS/PPE blends
 - glass transition temperature 272
- Q**
- quality of dispersion 247
 - nanoclay in PMMA 247
- R**
- reactively compatibilized blends
 - chemical reaction 356
 - distribution of compatibilizer 355
 - PA/SAN 355, 422
 - PS/PP 353, 420
 - reactively compatibilized PA/SAN blend
 - effect of compatibilizer on G' and G'' 356
 - recoverable compliance 108
 - influence of nanoclay 141
 - particle concentration 108
 - PMMA/carbon nanotubes 166
 - PMMA/graphite 160
 - PMMA/PS 329
 - stress dependence 132
 - recoverable elongation 336
 - PMMA/nanoclay 219
 - polyethylenes/glass fibers 218
 - PS/nanoclay 220
 - recoverable shear
 - HDPE/glass fibers 191
 - recoverable stretching ratio 337
 - PMMA/PS 343
 - PS/LLDPE 338
 - recovery experiment
 - cumulative particle distribution 398
 - morphology development 398
 - relaxation experiment
 - cumulative particle distribution 395
 - morphology development 395
 - PS/LLDPE 394

- retardation spectra 110
 - PMMA/nanoclay 141
 - PMMA with nanosilica 110
 - retardation strengths 111
 - retardation times 111
 - temperature dependence PMMA 128
 - temperature dependence PMMA/nanosilica 129
 - rheological measurements 2
 - definitions 5
 - experimental modes 5
 - stressing experiments 7
 - suspensions 35
 - rheological properties
 - acrylonitrile-butadiene-styrene copolymers (ABS) 306
 - carbon fillers 145
 - cocontinuous phase 344
 - compatibilized blends 349
 - compatibilized PS/PMMA 350
 - effect of surface area 117
 - filled thermoplastics 173
 - immiscible polymer blends 323
 - influence of matrix 119
 - influence of nanoparticles 93
 - PMMA/carbon nanotubes 165
 - PMMA/nanoclay 137
 - PP/carbon nanotubes 168
 - rubber-filled polymers (ABS) 305
 - rheometer
 - cone-and-plate 18
 - Couette 25
 - elongational 33
 - plate-plate 20
 - rheometry
 - capillary 26
 - rotational 18
- S**
- sample preparations 241
 - carbon-black composites 242
 - carbon nanotubes (MWCNT) 243
 - elongational experiments 432
 - graphite 242
 - laboratory kneader 430
 - nanoclay composites 241
 - polyethylene/glass beads 243
 - silica composites 241
 - SAN/PP blends
 - extrudate swell 330
 - morphology 331
 - morphology in capillary flow 331
 - sedimentation 46
 - glass beads 48
 - velocity 49
 - semicrystalline polymers 223
 - shear 6
 - shear rate 6
 - internal 70
 - shear stress 6
 - shear thickening 55
 - shear thinning 55
 - shift factor 17, 67
 - hydrodynamic regime 69, 72
 - slip 22, 26
 - capillary rheometer 32
 - Couette rheometer 26
 - rotational rheometer 22
 - slip of PVC 230
 - critical temperature 230
 - specific surface
 - particle size 98
 - Stoke's law 46
 - storage compliance 108
 - storage modulus
 - carbon black concentration 157
 - influence of carbon black 150
 - PMMA/carbon nanotubes 166
 - storage modulus of ABS
 - dependence on rubber content 318
 - strain hardening 203
 - particle shape 207
 - polypropylene blends 301
 - PS/LLDPE 333
 - retardation times 210
 - strain hardening of ABS
 - differently cross-linked rubber phase 313
 - strain thinning 210
 - ABS 314
 - structural heterogeneities 2
 - surface area of particles
 - creep experiments 118
 - creep recovery experiments 118
 - dynamic-mechanical experiments 118
 - suspensions 1
 - hydrodynamic regime 70
 - viscous behavior 59
- T**
- Taylor's theory 267
 - temperature dependence
 - PMMA/nanosilica 123
 - tensile stress 7
 - terminal regime 14

- thermal stability
 - ABS 427
 - ASA 427
 - carbon black composites 93, 148, 149
 - mass flow rate as function of time 427
 - nanosilica composites 96
 - PMMA/carbon nanotubes 165
 - PMMA/graphite 159
 - PMMA with different fillers 239
 - storage modulus 94
 - thermogravimetric analysis (TGA) 98
 - thermal stability of ABS
 - influence of rubber content 428
 - thermal stability of rubber-filled polymers
 - swelling index 429
 - thermodynamics of mixing 256
 - thermorheological behavior
 - complex 16
 - limits for investigations on miscibility 282
 - relation with mechanical spectra 280
 - simple 16
 - thermorheological behavior of polyethylenes
 - complexity 281
 - simplicity 281
 - van Gorp-Palmen plot 281
 - thermorheological complexity
 - dynamic-mechanical experiments 130
 - PMMA/nanosilica 126
 - thermorheological simplicity 126
 - thermorheological simplicity of polystyrene blends
 - van Gorp-Palmen plot 280
 - time-temperature shift factor 278
 - ABS 309
 - blends of polystyrenes 278
 - branched polystyrene 279
 - tip streaming 411
 - Tomotika theory 393
 - Trouton ratio 203
- U**
- uncompatibilized blends
 - cryofracture 412
 - uniaxial elongational
 - morphology of PS/LLDPE 376
- V**
- van der Waals potential 41, 42
 - viscosity 6
 - bidisperse suspensions 73
 - complex 13
 - elongational 7
 - influence of humidity 85
 - intrinsic 52
 - matrix fluid 67, 68
 - particle concentration 75
 - particle distribution 72
 - particle size 72, 75, 77
 - polydisperse particles 74
 - preshear 59
 - relative 52, 56
 - specific 52
 - specific surface 82
 - stress dependence 61
 - surface properties 83
 - temperature dependence 65
 - time dependence 59
 - zero-shear 9
 - viscosity functions 31, 57, 326
 - ABS copolymers 307
 - carbon black composites 151
 - filled polystyrene 175
 - filled thermoplastics 174
 - HDPE/glass fibers 178
 - LDPE/glass fibers 178
 - nanoparticles 100
 - numerical descriptions 179
 - PIB/PDMS 327
 - polyamide/glass fibers 177
 - polypropylene blends 301
 - polystyrene blends 289
 - PS 224
 - PVC 224
 - viscosity functions of PVC
 - temperature dependence 233
 - viscosity of filled wax
 - influence of humidity 195
 - viscosity ratio 264, 372
- W**
- Weissenberg-Rabinowitsch correction 30
 - WLF equation 17
- X**
- X-ray analysis for PS/LLDPE 444
 - X-ray diffraction
 - nanoclay 138
 - particle anisotropy 442
 - X-ray scattering intensities
 - PS/LLDPE 444
 - X-ray scattering (SAXS) 401
 - morphologies after relaxation 401

Y

yield stress 101, 152, 182, 198
- ABS 318

Z

zero-shear viscosity
- blending curves 287

- ethylene/olefin copolymers 298
- linear polyethylenes 297
- mixing rule 285
- particle concentration 108
- polyisobutylene blends 293
- prediction for homologous blends 288